

Article

Exploring the Impact of DAHP Impregnation on Activated Carbon Fibers for Efficient Charge Storage and Selective O₂ Reduction to Peroxide

Nemanja Gavrilov ¹, Stefan Breitenbach ^{2,3}, Christoph Unterweger ², Christian Fürst ²
and Igor A. Pašti ^{1,*}

- ¹ University of Belgrade—Faculty of Physical Chemistry, Studentski trg 12-16, 11158 Belgrade, Serbia; gavrilov@ffh.bg.ac.rs
- ² Wood K Plus—Kompetenzzentrum Holz GmbH, Altenberger Strasse 69, 4040 Linz, Austria; s.breitenbach@wood-kplus.at (S.B.); c.unterweger@wood-kplus.at (C.U.); c.fuerst@wood-kplus.at (C.F.)
- ³ Institute of Chemical Technology of Inorganic Materials (TIM), Johannes Kepler University Linz, Altenberger Strasse 69, 4040 Linz, Austria
- * Correspondence: igor@ffh.bg.ac.rs

Abstract: Understanding the properties and behavior of carbon materials is of paramount importance in the pursuit of sustainable energy solutions and technological advancements. As versatile and abundant resources, carbon materials play a central role in various energy conversion and storage applications, making them essential components in the transition toward a greener and more efficient future. This study explores the impact of diammonium hydrogen phosphate (DAHP) impregnation on activated carbon fibers (ACFs) for efficient energy storage and conversion applications. The viscose fibers were impregnated with varying DAHP concentrations, followed by carbonization and activation processes. The capacitance measurements were conducted in 6 mol dm⁻³ KOH, 0.5 mol dm⁻³ H₂SO₄, and 2 mol dm⁻³ KNO₃ solutions, while the oxygen reduction reaction (ORR) measurements were performed in O₂-saturated 0.1 mol dm⁻³ KOH solution. We find that the presented materials display specific capacitances up to 160 F g⁻¹ when the DAHP concentration is in the range of 1.0 to 2.5%. Moreover, for the samples with lower DAHP concentrations, highly selective O₂ reduction to peroxide was achieved while maintaining low ORR onset potentials. Thus, by impregnating viscose fibers with DAHP, it is possible to tune their electrochemical properties while increasing the yield, enabling the more sustainable and energy-efficient synthesis of advanced materials for energy conversion applications.

Keywords: activated carbon fibers; energy conversion; energy storage; oxygen reduction reaction



Citation: Gavrilov, N.; Breitenbach, S.; Unterweger, C.; Fürst, C.; Pašti, I.A. Exploring the Impact of DAHP Impregnation on Activated Carbon Fibers for Efficient Charge Storage and Selective O₂ Reduction to Peroxide. *C* **2023**, *9*, 105. <https://doi.org/10.3390/c9040105>

Academic Editors: Nikolaos Kostoglou and Claus Rebholz

Received: 2 September 2023

Revised: 26 October 2023

Accepted: 2 November 2023

Published: 6 November 2023



Copyright: © 2023 by the authors. Licensee MDPI, Basel, Switzerland. This article is an open access article distributed under the terms and conditions of the Creative Commons Attribution (CC BY) license (<https://creativecommons.org/licenses/by/4.0/>).

1. Introduction

Carbon materials play a pivotal role in the realm of energy conversion and storage owing to their exceptional properties, widespread availability, and versatility [1]. Their significance is underscored by their usage across various applications, including batteries [2,3], supercapacitors [4,5], fuel cells [6], solar cells [7], carbon capture [8,9], and hydrogen storage systems [10,11].

Some common properties of carbon materials are of high importance for different electrochemical applications. These include a high specific surface area, large porosity, and high conductivity [12]. However, the specific links between different properties and electrochemical performance have been elusive for a long time [13] and still remain a significant challenge for the research community. Irrespective of the complexity of such interlinks, carbon materials are multifunctional materials, and a single carbon material can find many different applications in electrochemical energy conversion and storage. The most direct possible application is in electrochemical capacitors. As there are no electrochemical reactions during the charging/discharging of an electrochemical capacitor, such systems can

deliver and store energy very fast, having higher power densities than batteries [14,15]. Thus, electrochemical capacitors can be used to complement battery systems in cases where short power bursts are needed. Many different types of carbon materials have found applications in electrochemical capacitors, like carbon nanotubes [16,17], graphene [17,18], carbon foam [19–21], and others. However, in many cases, the rationale for the use of complex carbon nanostructures is not well-justified. Most carbon materials, independent of their dimensionality, have capacitances up to 200–250 F g⁻¹. Thus, developing carbon materials using cheap and environmentally friendly sources using routes that do not require expensive and harmful chemicals should be the priority. In this sense, biomass-derived carbons present a particularly interesting class of carbon materials due to their structural diversity, renewability, wide availability, environmental friendliness, and low cost [22].

Carbon materials have found their place in electrocatalysis as well. Focusing particularly on fuel cell technologies, carbon materials have proven to be indispensable so far [23–25] for noble metal-based catalysts used on both the anode and cathode sides of low-temperature fuel cells. Focusing particularly on the cathode, where the oxygen reduction reaction (ORR) takes place, carbon materials are not very active ORR catalysts in acidic media but are rather good catalysts in alkaline solutions [26]. Moreover, the ORR can be boosted by introducing heteroatoms, such as nitrogen, boron, or phosphorus, into the carbon structure [27,28]. The introduction of heteroatoms can increase the activity and affect the selectivity of carbons in ORRs. Namely, the ORR is a complex electrochemical reaction that can proceed via a two-electron or four-electron pathway. In the first case, the reaction product is hydrogen peroxide (OH₂⁻ in alkaline media), while in the second case, it is water. The two-electron pathway is not desirable for fuel cell technologies as it leads to a lower power output (due to a lower number of electrons consumed per O₂) and possible damage to the system, particularly the membrane, by corrosive peroxide. However, this pathway can be utilized for the synthesis of hydrogen peroxide.

Hydrogen peroxide is one of the most frequently used chemicals in the world and has a growing billion-dollar market size [29]. Currently, its classical synthesis utilizes palladium-based catalysts [30], which are expensive and unsuitable for on-site peroxide generation. On the other hand, the electrochemical synthesis of hydrogen peroxide holds significant importance in the field of sustainable chemical production and environmental remediation, offering an alternative to traditional energy-intensive anthraquinone auto-oxidation processes [31,32]. Electrochemical synthesis offers a cleaner, more efficient, and selective route to H₂O₂ production [33]. This method involves the reduction of oxygen at the cathode, generating H₂O₂ as a primary product. The process can be fine-tuned by controlling parameters such as electrode material, electrolyte composition, and applied potential. This versatility enables the customization of the electrochemical process for various applications, from large-scale industrial production to on-site generation. In particular, electrochemical synthesis offers the advantage of directly producing H₂O₂ at the point of use, minimizing serious transportation, storage, and safety concerns associated with concentrated H₂O₂ solutions [34]. Nevertheless, the first step is identifying the materials with desired ORR selectivity.

To boost the electrochemical synthesis of hydrogen peroxide, catalysts favoring selective 2e-reduction are needed. Different classes of materials were tested for the electrochemical generation of H₂O₂. These include noble metals such as Ag and Au [35,36], oxide materials [37], and particularly, carbon-based materials [38–41]. Carbon materials are particularly suitable for peroxide synthesis as they possess a high chemical stability and can be tuned to favor the 2e-pathway. In this way, the electrochemical route to H₂O₂ synthesis can be stimulated, offering a greener alternative by reducing the environmental footprint compared to traditional H₂O₂ synthesis. Further benefits could be obtained by coupling electrochemical H₂O₂ synthesis with renewable energy sources like solar or wind power to enhance its sustainability further.

In this study, we analyze a series of well-characterized carbon materials in terms of their capacitive and electrocatalytic (ORR) performance. Specifically, we investigated

the effects of the synthesis conditions of diammonium hydrogen phosphate (DAHP)-impregnated viscose-based activated carbon fibers (ACFs) on their electrochemical performance. The systematic control of the amount of DAHP allowed for the continuous modification of the properties of the studied carbon materials, while increasing their yield significantly when compared to ACFs obtained without impregnation [42]. Considering the multifunctional nature of carbon materials, we have analyzed the capacitive and electrocatalytic properties of the presented series of materials. The capacitance was evaluated in alkaline ($6 \text{ mol dm}^{-3} \text{ KOH}$), pH-neutral ($2 \text{ mol dm}^{-3} \text{ KNO}_3$), and acidic solutions ($0.5 \text{ mol dm}^{-3} \text{ H}_2\text{SO}_4$). Moreover, the ORR was evaluated in an alkaline solution ($0.1 \text{ mol dm}^{-3} \text{ KOH}$) using the rotating disk electrode technique. We have discussed the role of the materials' properties, governed by specific synthetic conditions, on the electrochemical behavior of the studied ACFs. We find that in the analyzed series of materials, the best performance in terms of the capacitive response and selective O_2 reduction to hydrogen peroxide is obtained with intermediate concentrations of DAHP as the impregnation agent, while the specific links between the materials' properties and performance remained elusive.

2. Materials and Methods

2.1. Materials Synthesis and Characterization

The materials' synthesis (previously described in detail in [42]) involved drying viscose fibers (1.7 dtex, 38 mm) at $90 \text{ }^\circ\text{C}$ for 24 h, followed by impregnation in DAHP solutions of varying concentrations for 15 min. Carbonization was performed at $850 \text{ }^\circ\text{C}$ (heating rate $1 \text{ }^\circ\text{C min}^{-1}$, with an isothermal step for 20 min) under a nitrogen atmosphere, and subsequent activation occurred at $870 \text{ }^\circ\text{C}$ for 165 min in a CO_2 flow. The ACF samples are denoted as DAHP-X, where X represents the concentration of DAHP used. The synthesis steps are summarized in Scheme S1 (Supplementary Information).

The materials' characterization involved examining the ACF samples' morphology and elemental composition using a scanning electron microscope with energy-dispersive X-ray spectroscopy. Textural properties and specific surface area were determined via N_2 isothermal adsorption using the BET method and NLDFT, respectively [43,44]. Further details can be found in the previous works, in particular Refs. [42,45].

2.2. Capacitance Measurements

For the capacitance measurements, thin film electrodes were prepared through drop-casting of carbon ink. To begin, 5 mg of the desired carbon material was dispersed in a solution consisting of 400 μL of ethanol, 590 μL of deionized water, and 10 μL of a 0.5 wt% Nafion solution in ethanol. The mixture was then homogenized using ultrasound for 30 min to ensure uniformity. Next, films were formed by evaporating the solvent under a mild nitrogen gas stream from a 10 μL droplet of the carbon ink adhered to a glassy carbon (GC) disk electrode with a geometric surface area of 0.196 cm^2 . The specific mass loading was set at $250 \text{ } \mu\text{g cm}^{-2}$, which was crucial for the subsequent calculation of the materials' capacitance. Electrochemical measurements were performed in triplicate, starting with the electrode preparation and according to the descriptions provided below.

Electrochemical tests were conducted in a standard three-electrode setup, with a graphite rod serving as the counter electrode and a saturated calomel electrode (SCE) as a reference electrode. Cyclic voltammetry was employed to assess the capacitance of the tested materials in various solutions, including 6 mol dm^{-3} aqueous KOH, 0.5 mol dm^{-3} aqueous H_2SO_4 , and 2 mol dm^{-3} aqueous KNO_3 solutions. The Ivium VO1107 potentiostat/galvanostat was utilized for the measurements.

The gravimetric capacitances (C , in F g^{-1}) were calculated using the following formula:

$$C = \frac{Q}{2 \cdot \Delta V \cdot m} = \frac{\int i dt}{2 \cdot \Delta V \cdot m} \quad (1)$$

where Q represents the charge passed, obtained by integrating the positive and negative sweep in cyclic voltammograms. ΔV indicates the explored potential window, and m denotes the mass of the active material deposited on the surface of the GC electrode.

Before each experiment, the electrolyte was purged with nitrogen for 15 min to eliminate any potential contaminants. During the measurement, a gentle flow of nitrogen was maintained just below the electrolyte surface to ensure proper conditions. All measurements were performed at room temperature, precisely $(25.0 \pm 0.5) ^\circ\text{C}$.

2.3. ORR Measurements

The preparation of the electrodes for ORR measurements followed the same procedure as for the capacitance measurements. Briefly, the catalyst thin films were formed by evaporating the solvent under a mild nitrogen gas stream from a 10 μL droplet of the carbon catalyst ink drop-casted to a GC disk electrode with a geometric surface area of 0.196 cm^2 . The specific mass loading remained at $250 \mu\text{g cm}^{-2}$, as used in the capacitance measurements, ensuring consistency in the experimental setup. To investigate the oxygen reduction reaction (ORR) kinetics, the rotating disc electrode (RDE) technique was employed. The measurements were conducted in an O_2 -saturated 0.1 mol dm^{-3} KOH solution, which allowed for the accurate evaluation of the electrocatalytic activity of the carbon materials during the ORR process.

During the experiments, the electrolyte was carefully saturated with oxygen to create an oxygen-rich environment, promoting the ORR at the electrode surface. The RDE technique enabled precise control over the rotation rate of the electrode, ensuring a well-defined hydrodynamic condition for the measurements. Further data processing is elaborated on in Section 3: Results.

3. Results

The materials used in the present work have been extensively characterized and described in our previous works [42,45]. In the aforementioned works, one can find the scanning electron microscopy analysis, EDX data with mapping, specific surface area and pore size distribution measurements, and Raman and FTIR spectra of the described materials. For completeness, here, we present a brief summary of the materials' properties, necessary to discuss the materials' performances, while the representative results of the physical and chemical characterization can be found in Figure S1 (Supplementary Information).

Utilizing SEM, a consistent morphology across all the prepared activated carbon fiber samples was observed. This mirrors that of the precursor viscose fibers with an approximate 30% shrinkage, consistent with the prior findings of Breitenbach et al. [46]. During the milling of the samples, some ACFs remained intact, with lengths of up to 200 μm and a diameter of around 8 μm , while some ACFs fractured into smaller fragments.

Diverging from the uniform morphology, the chemical composition of ACFs demonstrated susceptibility to the loading of DAHP during impregnation (Table 1). As the amount of DAHP increased, the P content and, overall, the O content in the ACFs increased. Thus, by changing the amount of DAHP used in the impregnation step, it was possible to control the amount of P incorporated into the ACFs effectively. On the other hand, the increase in the oxygen content makes the surface more oxophilic, making the ACFs easier to disperse in water and obtain uniform catalyst films on the electrode.

Regarding the specific surface area (SSA) analysis, the sample that was not impregnated with DAHP showed a high SSA of nearly $2000 \text{ m}^2 \text{ g}^{-1}$. Then, the initial P-containing sample exhibited a considerable SSA decrease compared to the ACF sample without DAHP impregnation. However, the introduction of higher DAHP concentrations resulted in a subsequent SSA and total pore volume (V_{tot}) increase. Interestingly, the DAHP-2 sample deviated from this trend, showing a noticeably higher SSA compared to the samples with similar concentrations of DAHP used for the impregnation (1.5% and 2.5%). Moreover, the EDX findings showcased a heightened P fraction within its structure. Another interesting observation is that the pores shift towards larger radii as the DAHP concentration increases.

Namely, when the pore volume for the pores with a diameter under 1 nm is considered, there is clearly an overall decreasing trend in the $V_{1\text{nm}}$ as the DAHP concentration increases (Table 1). At the moment, we are not sure about the origin of these deviations from the overall trends when the DAHP concentration is between 1.5 and 2.5%. However, tuning the physical and chemical properties of the studied ACFs in a relatively wide and controllable way can help not only identify the most suitable materials for the desired applications but also draw some general conclusions regarding the impact of the materials' properties on their electrochemical behavior.

Table 1. Adsorbents properties—pore volume integrated up 1 nm, total pore volume (integrated up to $d_p = 35$ nm, V_{tot}), surface area (S_{tot}), and elemental content determined using energy-dispersive X-ray spectroscopy. The notation of samples is DAHP-X, where X represents the amount of DAHP used for the impregnation step. Reproduced from [42]. This work is published with Open Access under Creative Commons License.

X=	0.00%	0.25%	0.50%	1.00%	1.50%	2.00%	2.50%	5.00%	7.50%	10%	
$V_{1\text{nm}}/\text{cm}^3 \text{g}^{-1}$	0.348	0.335	0.339	0.343	0.297	0.271	0.274	0.198	0.137	0.160	
$V_{\text{tot}}/\text{cm}^3 \text{g}^{-1}$	0.757	0.383	0.472	0.774	0.770	1.094	0.833	1.291	1.681	1.322	
$S_{\text{tot}}/\text{m}^2 \text{g}^{-1}$	1932	1016	1250	2037	2002	2556	2018	2718	2763	2718	
Elemental Content	C/at.%	92.4 ± 2.1	91.6 ± 3.5	93.6 ± 2.3	87.9 ± 1.3	93.9 ± 1.9	91.3 ± 2.0	87.9 ± 2.0	85.6 ± 2.5	82.2 ± 2.2	77.8 ± 5.0
	O/at.%	7.6 ± 2.0	8.4 ± 3.5	6.2 ± 2.2	12 ± 1.3	5.9 ± 1.9	7.7 ± 2.3	11.4 ± 2.2	13.1 ± 2.7	16.1 ± 2.3	19.7 ± 5.3
	P/at.%	0	0.02 ± 0.02	0.18 ± 0.10	0.11 ± 0.04	0.28 ± 0.07	0.91 ± 0.29	0.65 ± 0.30	1.32 ± 0.34	1.78 ± 0.13	1.9 ± 0.64

First, we present the results of the capacitance measurements. Figure 1 (top row) shows the capacitive responses of the DAHP-2.0 sample in three different electrolytes. As we have used the SCE electrode as a reference electrode, the potential window in which cycling was performed is shifted to higher potentials as the pH of the electrolytic solution decreases. It is clear that the capacitive response is nearly rectangular in shape, without significant features like voltammetry peaks that would indicate pseudo-faradaic or faradic behavior. The overall capacitive response considering the different electrolytic solutions increases in the following order: $\text{KNO}_3 \approx \text{H}_2\text{SO}_4 < \text{KOH}$. Such a trend is clearly seen from the comparison of the specific capacitances measured for the entire series at a common potential sweep rate of 100 mV s^{-1} (Figure 1, bottom row). Overall, considering the capacitances measured at 100 mV s^{-1} , for the entire series, the values range between 35 and 160 F g^{-1} , demonstrating a great variety of the capacitive properties of the studied materials. This result is not overly surprising, considering that the chemical composition and the textural properties of the studied carbon materials also vary to a significant extent. However, while the properties of the studied carbons change progressively with the amount of DAHP used in the synthesis, the capacitive properties do not show such a trend, and the capacitance is maximized for the samples prepared with a relatively low amount of impregnating agent (1.0% to 2.5%).

Table 2 summarizes the measured capacitances of all the samples for potential sweep rates from 5 to 400 mV s^{-1} in 6 mol dm^{-3} KOH solution. For the KNO_3 and H_2SO_4 solutions, the data are given in the Supplementary Information, Table S1 and S2. Figure 2 presents the overall trends in the measured capacitances.

Table 2. Measured capacitances (F g^{-1}) in 6 mol dm^{-3} KOH solution at different scan rates.

Material	5 mV s^{-1}	10 mV s^{-1}	20 mV s^{-1}	50 mV s^{-1}	100 mV s^{-1}	200 mV s^{-1}	400 mV s^{-1}
0.0% DAHP	84.5 ± 6.8	87.6 ± 6.1	89.4 ± 6.3	87.2 ± 5.2	75.5 ± 4.5	69.1 ± 4.1	59.5 ± 4.2
0.25% DAHP	94.6 ± 7.6	88.4 ± 4.4	82.2 ± 4.1	70.9 ± 4.3	56.6 ± 3.4	46.0 ± 2.8	36.6 ± 2.9
0.5% DAHP	87.8 ± 7.9	78.1 ± 6.2	75.8 ± 4.5	74.9 ± 3.0	62.6 ± 2.5	57.7 ± 2.3	51.9 ± 2.6
1.0% DAHP	133 ± 7	149 ± 10	168.2 ± 6.7	174 ± 11	159 ± 8	151 ± 11	138 ± 11

Table 2. Cont.

Material	5 mV s ⁻¹	10 mV s ⁻¹	20 mV s ⁻¹	50 mV s ⁻¹	100 mV s ⁻¹	200 mV s ⁻¹	400 mV s ⁻¹
1.5% DAHP	192 ± 8	137.3 ± 6.9	144 ± 7	148.0 ± 5.9	135.0 ± 8.1	128.2 ± 6.4	118.1 ± 9.4
2.0% DAHP	125 ± 11	146 ± 6	168 ± 7	173 ± 7	156.2 ± 7.8	150 ± 14	138 ± 11
2.5% DAHP	141.9 ± 8.5	152.2 ± 6.1	166 ± 10	167 ± 10	153.0 ± 6.1	142.8 ± 5.7	128.9 ± 6.4
5.0% DAHP	92.5 ± 7.4	93.0 ± 7.4	113.0 ± 4.5	126.0 ± 6.3	112.7 ± 7.9	112.4 ± 7.9	107.4 ± 7.5
7.5% DAHP	91.4 ± 3.7	77.8 ± 6.2	84.2 ± 5.9	88.9 ± 5.3	78.3 ± 4.7	75.2 ± 6.0	69.7 ± 4.9
10.0% DAHP	124.7 ± 7.5	107.3 ± 6.4	110.7 ± 6.6	115.4 ± 8.1	99.8 ± 4.0	96.9 ± 8.7	91.5 ± 6.4

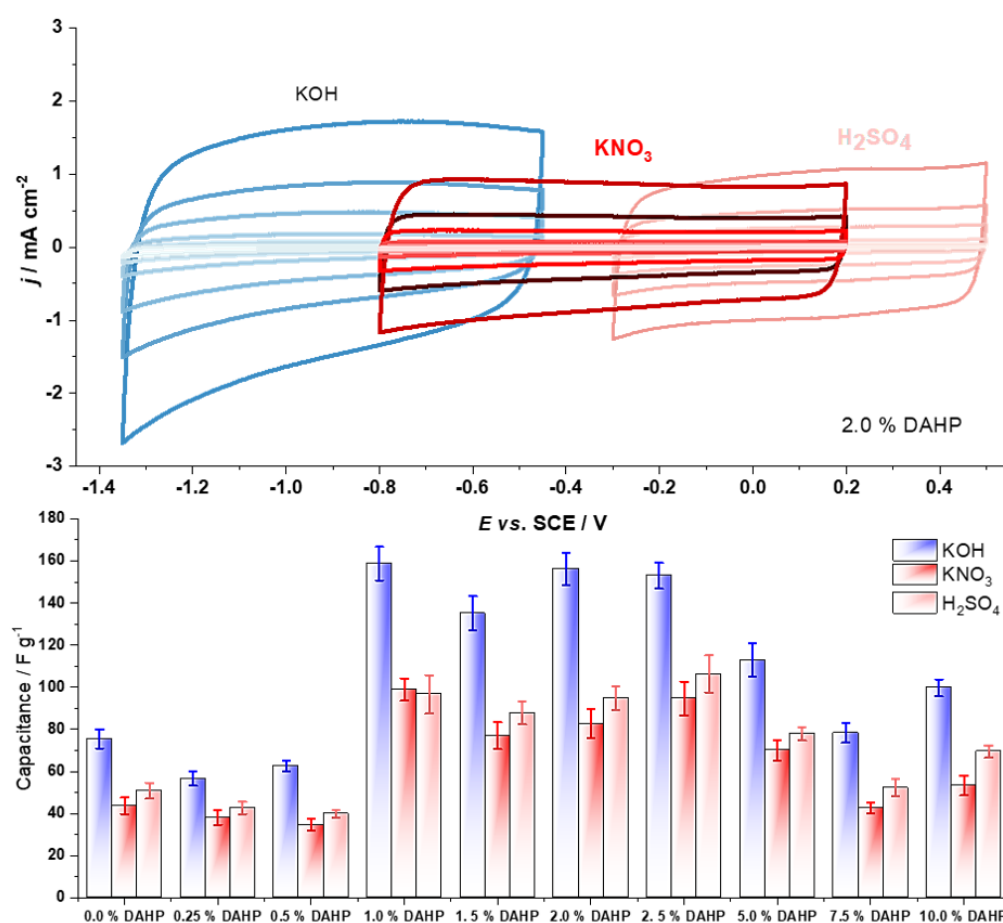


Figure 1. Top row—cyclic voltammograms of 2.0% DAHP sample at different scan rates and electrolytes at a common potential sweep rate of 100 mV s⁻¹; bottom row—measured capacitances at a potential scan rate of 100 mV s⁻¹ in different electrolytes (quiescent and N₂-purged).

As can be seen from the presented data, Figure 1 (bottom row), and Figure 2, the samples in the middle of the series with a DAHP concentration ranging from 1.0 to 2.5% stand out as the ones with the highest capacitive responses in all three electrolytes. This finding immediately draws to the conclusion that the SSA is not the primary factor that determines the capacitive response, as the highest SSA is reached for the materials impregnated with high concentrations of DAHP.

Next, we turn to the ORR activity measurements. First, we compare the background curves, i.e., the capacitive responses in 0.1 mol dm⁻³ KOH (Figure 3, left). The baselines suggest that the used electrolyte's electrochemically accessible surface differs from sample to sample and follows the trends in the measured capacitances in the concentrated KOH solution. Upon introducing O₂ in the solution, the ORR current was measured (Figure 3,

middle) at different electrode rotation rates (Figure 3, right). The onset potentials for some of the materials were found to be rather high, above -0.2 V vs. SCE (i.e., above 0.8 V vs. RHE), with the sample denoted as 2.5% DAHP having the highest activity considering the current response. Further, to precisely evaluate the activity and selectivity of the studied materials, we have used Koutecky–Levich (K–L) analysis [47].

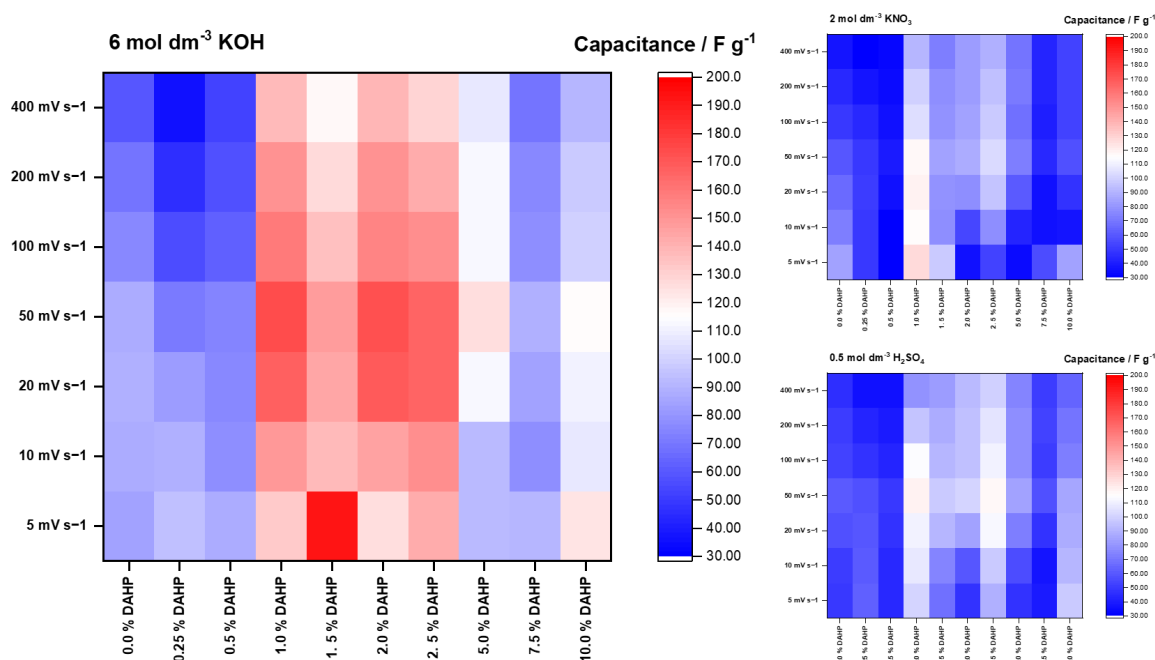


Figure 2. Heatmaps for measured capacitances in three different solutions, as indicated in the plots. The potential sweep rate was between 5 and 400 mV s^{-1} . The color map and the scale are the same for all three electrolytes, which clearly shows that the capacitances are the highest in the 6 mol dm^{-3} KOH solution.

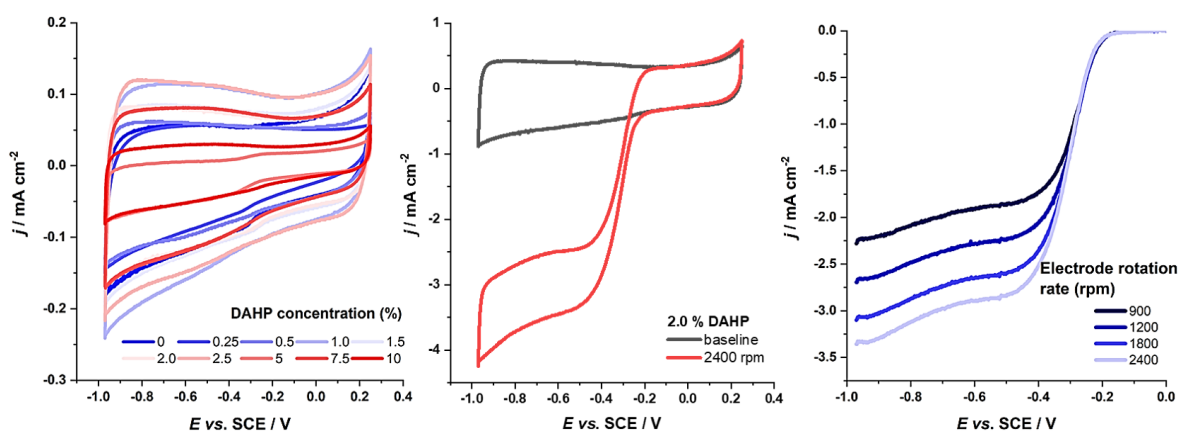


Figure 3. Left—baselines for the investigated materials in de-aerated 0.1 mol dm^{-3} KOH, potential sweep rate 20 mV s^{-1} ; middle—raw ORR current (at the electrode rotation rate of 2400 rpm) and the background current of the DAHP-2.0 sample; right—background-corrected ORR currents of 2.5% DAHP sample, measured at different electrode rotation rates (in rpm, indicated in the figure).

In the K–L analysis, the measured current densities (j) can be presented as (see Figure S2, Supplementary Information

$$\frac{1}{j} = \frac{1}{j_k} + \frac{1}{j_d} \quad (2)$$

where j_k and j_d are the kinetic current and limiting diffusion current, respectively. The kinetic current depends primarily on the electrode potential, while the diffusion current depends on the number of electrons transferred per O_2 molecule (n) and the electrode rotation rate (ω) as $j_d = n \times B \times \omega^{1/2}$. B is a constant that assembles other parameters such as the O_2 concentration, kinematic viscosity of the solution, and other relevant parameters that were constant during our measurements [47]. Once we extracted the kinetic current densities, we normalized them to the mass of the ACFs deposited on the electrode (by dividing j_k with the catalyst loading), thus obtaining mass-specific activities at different electrode potentials (Table S3, Supplementary Information). The calculated numbers of electrons consumed per O_2 molecule are summarized in the Supplementary Information, Table S4.

The number of electrons and the kinetic current are mutually interconnected, as determined in the K–L analysis from the slope and the intercept of the K–L plot (Equation (2)). Figure 4 (top row) summarizes the mass activities (in $A\ g^{-1}$) at two different electrode potentials (-0.4 and -0.6 V vs. SCE), while Figure 4 (bottom row) presents the dependence of the number of electrons per O_2 molecule on the electrode potential for the entire series of ACFs. We have not observed a particular trend along the series considering the mass activities, while the samples with lower concentrations of DAHP (thus P and O, Table 1) show a somewhat lower number of electrons transferred per O_2 molecule, thus show a better selectivity for peroxide formation. Nevertheless, the samples in the middle of the series, which exhibited the highest capacitances in alkaline solution (Figure 2), do show the highest ORR mass activities. However, the overall trends in the capacitances and ORR mass activities are not the same.

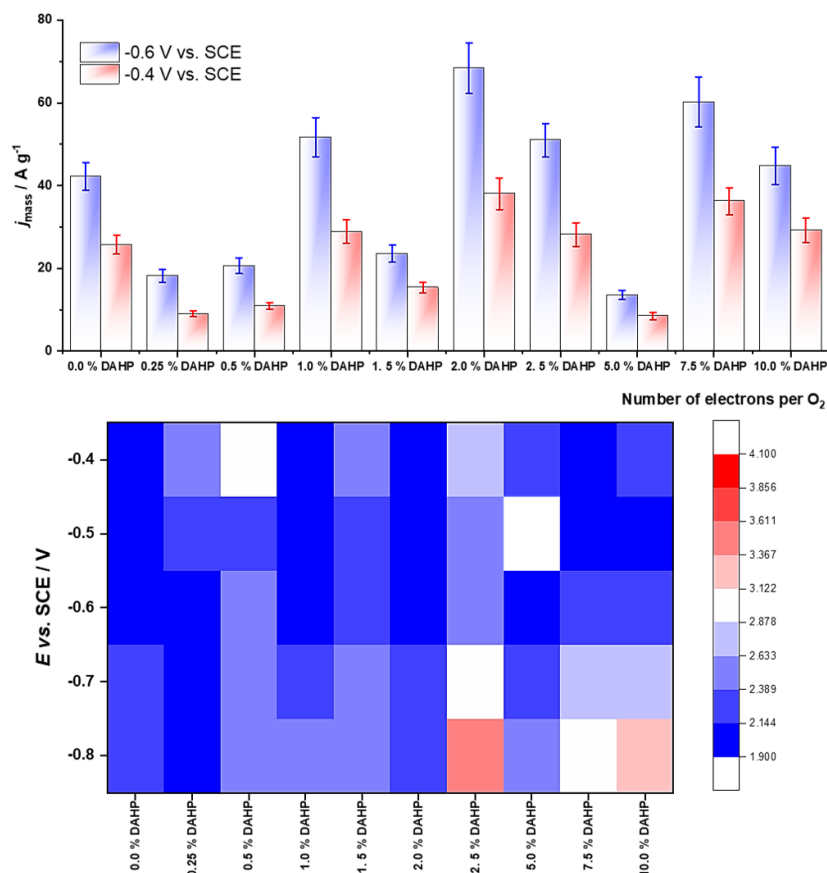


Figure 4. **Top row**—ORR mass activities of investigated samples at -0.4 and -0.6 V vs. SCE, calculated from the anodic scan; **bottom row**—number of electrons consumed per O_2 molecule, in the potential range -0.4 to -0.8 V vs. SCE.

4. Discussion

Overall, in the analysis of the measured capacitance, we observed some irregular behavior concerning its dependence on the scan rate, particularly a decrease in the capacitance at low potential sweep rates. Notably, this effect is no longer evident at high potential scan rates. Based on our findings, we can conclude that the capacitance is maximized for DAHP concentrations ranging between 1% and 2.5%. Furthermore, we noticed a consistent trend in the capacitance values across different electrolytes, with KOH exhibiting the highest capacitance. The cyclic voltammograms displayed a well-defined capacitive behavior for most of the tested materials, further supporting the observed high capacitance in alkaline media. Our results align with our previous experiences involving various carbon materials, where high capacitances were consistently observed to be the highest in an alkaline environment [48–51]. In the analysis of the ORR activity, we observed variations in the catalytic activity along the series but without any particular trend that can be outlined. Notably, among the tested materials, the sample denoted as DAHP-2.0 exhibited the highest ORR activity, measured as mass activity. When considering the entire series of materials, we did not observe any prominent plateau with increasing the DAHP content, but rather variations in electrochemical response, which are more prominent in the case of the ORR activity (Figure 4). In the case of the capacitive response (Figure 1) one could hypothesize that the DAHP content above 2.5% starts to have a detrimental effect on the capacitance, either because the pores become too large or the surface chemistry is altered in undesirable ways. However, such a hypothesis cannot be valid for the case of the ORR activity as the activity oscillates along the series. Next, we discuss the connection between the materials' properties and their electrochemical behavior.

In the analysis of the properties–performance link, we have investigated the correlation of the different materials' properties, as summarized in Table 1, and the results of the electrochemical investigation. Strikingly, while the materials' properties, like the O content, SSA, and pore volumes, are mutually interconnected, their link with the materials' performance is missing (Figure 5). The consistency between the measured capacitances in different electrolytes was observed, showing that the overall trends in the capacitances are preserved in different electrolytes. However, we have failed to find any properties that can be significantly correlated to the ORR activity and measured capacitances. Moreover, the attempt to use the linear combinations of materials' properties through the multiple linear regression approach was also not successful. Likely, there is a very complex property–performance dependence that cannot be outlined in a simple way. This urges further research in an attempt to reveal the deep links between the materials' structure and electrochemical performance.

Nevertheless, the samples with relatively low amounts of DAHP (1.0 to 2.5%) stand out as materials with a high capacitance and also high ORR activity. Moreover, the same materials displayed a high selectivity of O₂ reduction to peroxide. The DAHP-2.0 sample displayed a high capacitance in alkaline solutions (up to approx. 170 F g⁻¹) and up to 100 F g⁻¹ in acidic solutions. The same sample showed mass activity of more than 60 A g⁻¹ at high ORR overpotentials (−0.8 V vs. SCE) and a very good selectivity of O₂ reduction to peroxide. Namely, the calculated number of electrons consumed per O₂ was between 2.06 and 2.35 in the potential range from −0.4 to −0.8 V vs. SCE. Notably, there were a few more samples with relatively high mass activities and good selectivity for peroxide formation, especially at higher potentials (lower ORR overpotentials). These include the DAHP-0, DAHP-1.0, and DAHP-7.5 samples. On the other hand, the DAHP-2.5 sample showed the highest *n*, setting itself as the most active material for O₂ reduction to water (hydroxyl ions). Considering that the ACF yields are significantly improved upon the impregnation with DAHP [52,53] and that the ORR onset potentials are quite high (above 0.8 V vs. RHE, that is, above −0.2 V vs. SCE), the described ACF synthesis seems to be a viable strategy to obtain highly efficient ORR catalysts with a potential to be used in the electrochemical synthesis of hydrogen peroxide. However, the present results should be taken with care regarding the actual use of the studied materials for electrochemical

hydrogen peroxide synthesis, and additional work is needed, particularly determining the H_2O_2 yield under relevant synthesis conditions and determining the catalysts' stability under prolonged operation.

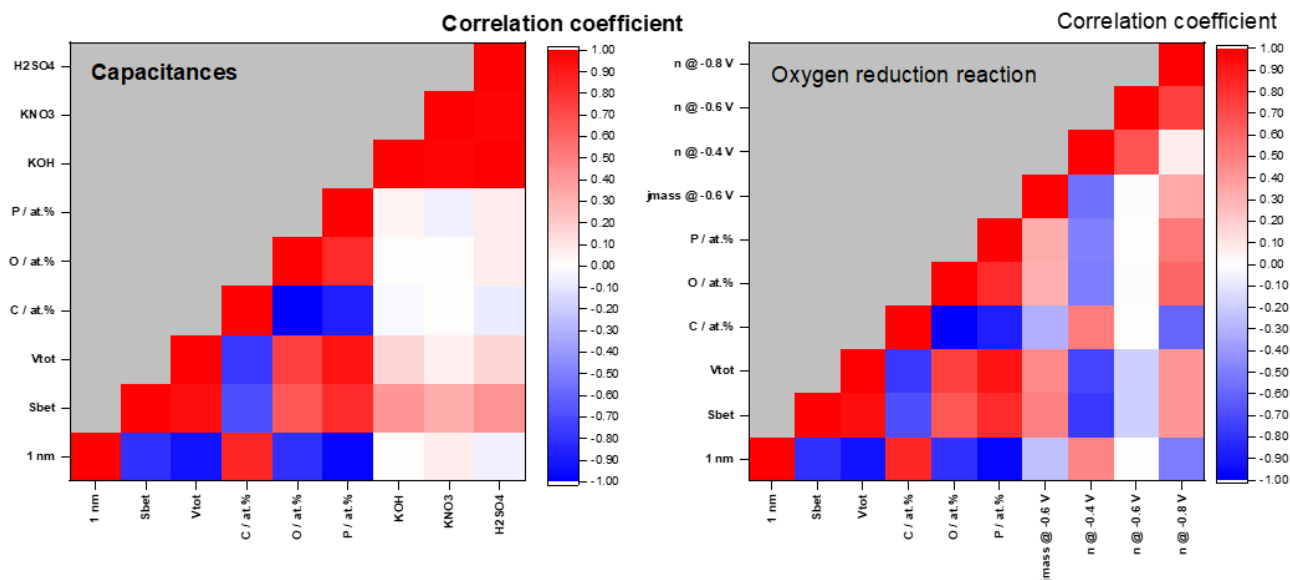


Figure 5. Pearson's correlation coefficient matrix linking capacitance (**left**) and ORR activity and selectivity (**right**) with materials properties.

We note that the capacitive applications of carbon materials usually relate to their electrochemistry in non-aqueous solutions. This is because the energy density of an electrochemical capacitor is not only a linear function of the gravimetric capacitance but also a square function of the voltage window. In this way, by making a wider window of the electrochemical stability of capacitive material and the electrolyte, one can significantly increase the energy density of the capacitor. Moreover, the electrochemical capacitor market is predominantly populated with devices containing non-aqueous electrolytes (usually with an upper voltage limit of approximately 2.7 V), but the majority of fundamental studies are performed in aqueous electrolytes. Part of the presented series of materials has already been analyzed in terms of the capacitance in a non-aqueous electrolyte [53]. In that study, the capacitances up to 139 F g^{-1} were measured; thus, they were somewhat lower compared to the values measured here in KOH solution but higher compared to the ones measured in the H_2SO_4 and KNO_3 solutions. Moreover, just like the present study, the measured capacitances were not possible to uniquely link to some of the specific materials' properties, like the SSA or pore volume. To make the situation more complicated, the maximum capacitance in non-aqueous solutions was observed for the sample with the highest concentration of P, while, here, we see the maximum capacitance for the DAHP-2.0 sample. This particular sample was indicated to stand out by a high SSA and higher P content than one could expect on the basis of the initial DAHP concentration used for impregnation. Thus, not only do the links between the carbon materials' properties and their electrochemical performance remain elusive but also the electrochemical performance in aqueous and non-aqueous solutions does not correlate mutually.

5. Conclusions

In this study, the impact of DAHP impregnation in the production of viscose-derived ACFs for electrochemical applications was investigated. The DAHP concentration significantly influences the capacitance of the ACFs, with an optimum range of 1.0% to 2.5%. Furthermore, the highest capacitance was consistently achieved in the KOH electrolyte, followed by H_2SO_4 , and finally KNO_3 . The analysis of the ORR activity indicated that some materials exhibited high onset potentials, exceeding -0.2 V vs. SCE. Particularly, the

DAHP-2.0 sample displayed the highest activity among the tested materials, expressed in terms of mass activity. As a particularly important finding, we emphasize the high selectivity of O₂ reduction to peroxide, which can be utilized for the electrochemical synthesis of hydrogen peroxide. Several materials in the investigated series, including the most active, the DAHP-2.0 sample, displayed the almost complete O₂ reduction to peroxide, with the number of transferred electrons per O₂ molecule practically matching two at higher potentials. Considering the fine-tuning and optimization of the materials' properties, the obtained results suggest that the DAHP concentration range from 1.0 to 2.5% should be investigated in more detail. Our attempts to link the materials' properties and their electrochemical performances were unsuccessful, making these links elusive. Moreover, we could not correlate the capacitances measured in aqueous solutions with those measured in non-aqueous electrolytes. This leads to the conclusion that specific interactions governing high capacitive responses in aqueous and non-aqueous electrolytes are different. While the present study did not allow for the deep link between the physicochemical properties of materials and their electrochemical behavior, it clearly emphasizes the positive role of DAHP impregnation on tuning the ACFs' electrochemical behavior in terms of the capacitive response and ORR activity and selectivity. Combining these findings with a significant increase in ACF yields when the DAHP impregnation step is used, it is clear that the demonstrated approach could lead to more energy-efficient and sustainable routes for producing advanced materials with desirable electrochemical properties.

Supplementary Materials: The following supporting information can be downloaded at: <https://www.mdpi.com/article/10.3390/c9040105/s1>, Scheme S1: The block synthesis workflow for the DAHP-X samples; Figure S1: The representative results of the physical and chemical characterization of the studied samples: top row—Raman spectrum and Pore Size Distribution for selected samples, middle row—Scanning Electron Microscopy Analysis, bottom row—EDX mapping for the sample 2% DAHP; Figure S2: Representative Koutecky-Levich plots of studied ACF samples: (a) sample 2.0% DAHP, (b) sample 2.5% DAHP; Table S1: Measured capacitances (F g⁻¹) in H₂SO₄ solution at different scan rates; Table S2: Measured capacitances (F g⁻¹) in KNO₃ solution at different scan rates; Table S3: Calculated ORR mass activities (in A g⁻¹); Table S4: Number of electrons consumed *per* O₂ molecule, calculated at different electrode potentials.

Author Contributions: Conceptualization, N.G., S.B., C.U., C.F. and I.A.P.; formal analysis, N.G., S.B. and I.A.P.; funding acquisition, C.F. and I.A.P.; investigation, N.G. and S.B.; methodology, N.G., S.B., C.U., C.F. and I.A.P.; project administration, C.F.; resources, C.U.; supervision, C.U. and C.F.; validation, S.B. and C.U.; writing—original draft, N.G., S.B. and I.A.P.; writing—review and editing, C.U., C.F. and I.A.P. All authors have read and agreed to the published version of the manuscript.

Funding: S.B., C.U. and C.F. gratefully acknowledge financial support through the COMET Programme (Competence Centers for Excellent Technologies) funded by the Austrian ministries BMK, BMAW, and the federal states of Upper Austria, Lower Austria, and Carinthia, operated by the Austrian Research Promotion Agency (FFG). I.A.P. and N.G. acknowledge the support provided by the Serbian Ministry of Education, Science, and Technological Development (Contract number: 451-03-47/2023-01/200146).

Data Availability Statement: The data are contained within the article.

Conflicts of Interest: The authors declare no conflict of interest.

References

1. Zhang, Y.; Li, C.; Cao, F.; Noori, A.; Mousavi, M.F.; Xia, X. Carbon in Electrochemical Energy. *Mater. Res. Bull.* **2022**, *152*, 111852. [[CrossRef](#)]
2. Wu, Z.; Sun, K.; Wang, Z. A Review of the Application of Carbon Materials for Lithium Metal Batteries. *Batteries* **2022**, *8*, 246. [[CrossRef](#)]
3. Yang, S.; Cheng, Y.; Xiao, X.; Pang, H. Development and Application of Carbon Fiber in Batteries. *Chem. Eng. J.* **2020**, *384*, 123294. [[CrossRef](#)]
4. Wang, Y.; Zhang, L.; Hou, H.; Xu, W.; Duan, G.; He, S.; Liu, K.; Jiang, S. Recent Progress in Carbon-Based Materials for Supercapacitor Electrodes: A Review. *J. Mater. Sci.* **2021**, *56*, 173–200. [[CrossRef](#)]

5. Zhai, Z.; Zhang, L.; Du, T.; Ren, B.; Xu, Y.; Wang, S.; Miao, J.; Liu, Z. A Review of Carbon Materials for Supercapacitors. *Mater. Des.* **2022**, *221*, 111017. [[CrossRef](#)]
6. Jaleh, B.; Nasrollahzadeh, M.; Eslamipannah, M.; Nasri, A.; Shabanlou, E.; Manwar, N.R.; Zboril, R.; Fornasiero, P.; Gawande, M.B. The Role of Carbon-Based Materials for Fuel Cells Performance. *Carbon* **2022**, *198*, 301–352. [[CrossRef](#)]
7. Hadadian, M.; Smått, J.-H.; Correa-Baena, J.-P. The Role of Carbon-Based Materials in Enhancing the Stability of Perovskite Solar Cells. *Energy Environ. Sci.* **2020**, *13*, 1377–1407. [[CrossRef](#)]
8. Abd, A.A.; Othman, M.R.; Kim, J. A Review on Application of Activated Carbons for Carbon Dioxide Capture: Present Performance, Preparation, and Surface Modification for Further Improvement. *Environ. Sci. Pollut. Res.* **2021**, *28*, 43329–43364. [[CrossRef](#)] [[PubMed](#)]
9. Liu, E.; Lu, X.; Wang, D. A Systematic Review of Carbon Capture, Utilization and Storage: Status, Progress and Challenges. *Energies* **2023**, *16*, 2865. [[CrossRef](#)]
10. Bader, N.; Ouederni, A. Optimization of Biomass-Based Carbon Materials for Hydrogen Storage. *J. Energy Storage* **2016**, *5*, 77–84. [[CrossRef](#)]
11. Mohan, M.; Sharma, V.K.; Kumar, E.A.; Gayathri, V. Hydrogen Storage in Carbon Materials—A Review. *Energy Storage* **2019**, *1*, e35. [[CrossRef](#)]
12. Pang, T.; Marken, F.; Zhang, D.; Mattia, D.; Shen, J. Linking Macroscopic Surface Morphology of Activated Carbon Fibres and Electrodesorption Performance: An Electrochemical Impedance Spectroscopy and Capacitive Deionization Study. *Appl. Surf. Sci.* **2023**, *609*, 155397. [[CrossRef](#)]
13. Pašti, I.A.; Janošević Ležaić, A.; Gavrilov, N.M.; Ćirić-Marjanović, G.; Mentus, S.V. Nanocarbons Derived from Polymers for Electrochemical Energy Conversion and Storage—A Review. *Synth. Met.* **2018**, *246*, 267–281. [[CrossRef](#)]
14. Winter, M.; Brodd, R.J. What Are Batteries, Fuel Cells, and Supercapacitors? *Chem. Rev.* **2004**, *104*, 4245–4270. [[CrossRef](#)] [[PubMed](#)]
15. Rani, J.; Thangavel, R.; Oh, S.-I.; Lee, Y.; Jang, J.-H. An Ultra-High-Energy Density Supercapacitor; Fabrication Based on Thiol-Functionalized Graphene Oxide Scrolls. *Nanomaterials* **2019**, *9*, 148. [[CrossRef](#)] [[PubMed](#)]
16. Felhősi, I.; Keresztes, Z.; Marek, T.; Pajkossy, T. Properties of Electrochemical Double-Layer Capacitors with Carbon-Nanotubes-on-Carbon-Fiber-Felt Electrodes. *Electrochim. Acta* **2020**, *334*, 135548. [[CrossRef](#)]
17. Frackowiak, E.; Jurewicz, K.; Delpeux, S.; Beguin, F. Electrochemical Application of Carbon Nanotubes. In *Low-Dimensional Systems: Theory, Preparation, and Some Applications*; Springer: Dordrecht, The Netherlands, 2003; pp. 305–318.
18. Chen, J.; Li, C.; Shi, G. Graphene Materials for Electrochemical Capacitors. *J. Phys. Chem. Lett.* **2013**, *4*, 1244–1253. [[CrossRef](#)]
19. Udayakumar, M.; Tóth, P.; Wiinikka, H.; Malhotra, J.S.; Likozar, B.; Gyergyek, S.; Leskó, A.K.; Thangaraj, R.; Németh, Z. Hierarchical Porous Carbon Foam Electrodes Fabricated from Waste Polyurethane Elastomer Template for Electric Double-Layer Capacitors. *Sci. Rep.* **2022**, *12*, 11786. [[CrossRef](#)] [[PubMed](#)]
20. Cao, M.; Feng, Y.; Tian, R.; Chen, Q.; Chen, J.; Jia, M.; Yao, J. Free-Standing Porous Carbon Foam as the Ultralight and Flexible Supercapacitor Electrode. *Carbon* **2020**, *161*, 224–230. [[CrossRef](#)]
21. Park, H.; Seo, J.; Kim, M.; Baeck, S.-H.; Shim, S.E. Development of a Carbon Foam Supercapacitor Electrode from Resorcinol-Formaldehyde Using a Double Templating Method. *Synth. Met.* **2015**, *199*, 121–127. [[CrossRef](#)]
22. Zhang, Y.; Pan, H.; Zhou, Q.; Liu, K.; Ma, W.; Fan, S. Biomass-Derived Carbon for Supercapacitors Electrodes—A Review of Recent Advances. *Inorg. Chem. Commun.* **2023**, *153*, 110768. [[CrossRef](#)]
23. Lam, E.; Luong, J.H.T. Carbon Materials as Catalyst Supports and Catalysts in the Transformation of Biomass to Fuels and Chemicals. *ACS Catal.* **2014**, *4*, 3393–3410. [[CrossRef](#)]
24. Rodríguez-Reinoso, F.; Sepúlveda-Escribano, A. Carbon as Catalyst Support. In *Carbon Materials for Catalysis*; John Wiley & Sons, Inc.: Hoboken, NJ, USA, 2008; pp. 131–155.
25. Trogadas, P.; Fuller, T.F.; Strasser, P. Carbon as Catalyst and Support for Electrochemical Energy Conversion. *Carbon* **2014**, *75*, 5–42. [[CrossRef](#)]
26. Ma, R.; Lin, G.; Zhou, Y.; Liu, Q.; Zhang, T.; Shan, G.; Yang, M.; Wang, J. A Review of Oxygen Reduction Mechanisms for Metal-Free Carbon-Based Electrocatalysts. *NPJ Comput. Mater.* **2019**, *5*, 78. [[CrossRef](#)]
27. Taguchi, T.; Gohda, S.; Gotoh, K.; Sato, S.; Yamada, Y. Synthesis of Carbon Materials with Extremely High Pyridinic-Nitrogen Content and Controlled Edges from Aromatic Compounds with Highly Symmetric Skeletons. *Carbon Lett.* **2023**, *33*, 1279–1301. [[CrossRef](#)]
28. Pašti, I.A.; Gavrilov, N.M.; Dobrota, A.S.; Momčilović, M.; Stojmenović, M.; Topalov, A.; Stanković, D.M.; Babić, B.; Ćirić-Marjanović, G.; Mentus, S.V. The Effects of a Low-Level Boron, Phosphorus, and Nitrogen Doping on the Oxygen Reduction Activity of Ordered Mesoporous Carbons. *Electrocatalysis* **2015**, *6*, 498–511. [[CrossRef](#)]
29. Tuci, G.; Rossin, A.; Zhang, X.; Truong-Phuoc, L.; Berretti, E.; Liu, Y.; Pham-Huu, C.; Ali, S.; Jan, F.; Poggini, L.; et al. Metal-Free Electrocatalysts for the Selective 2 e⁻ Oxygen Reduction Reaction: A Never-Ending Story? *Chem.—Eur. J.* **2023**, *29*, e202301036. [[CrossRef](#)] [[PubMed](#)]
30. Campos-Martin, J.M.; Blanco-Brieva, G.; Fierro, J.L.G. Hydrogen Peroxide Synthesis: An Outlook beyond the Anthraquinone Process. *Angew. Chemie Int. Ed.* **2006**, *45*, 6962–6984. [[CrossRef](#)] [[PubMed](#)]
31. Foller, P.C.; Bombard, R.T. Processes for the Production of Mixtures of Caustic Soda and Hydrogen Peroxide via the Reduction of Oxygen. *J. Appl. Electrochem.* **1995**, *25*, 613–627. [[CrossRef](#)]

32. Gopal, R. Electrochemical Synthesis of Hydrogen Peroxide. U.S. Patent 20030019758A1, 30 March 2004.
33. Perry, S.C.; Pangotra, D.; Vieira, L.; Csepei, L.-I.; Sieber, V.; Wang, L.; Ponce de León, C.; Walsh, F.C. Electrochemical Synthesis of Hydrogen Peroxide from Water and Oxygen. *Nat. Rev. Chem.* **2019**, *3*, 442–458. [[CrossRef](#)]
34. Yang, S.; Verdaguer-Casadevall, A.; Arnarson, L.; Silvioli, L.; Čolić, V.; Frydendal, R.; Rossmeisl, J.; Chorkendorff, I.; Stephens, I.E.L. Toward the Decentralized Electrochemical Production of H₂O₂: A Focus on the Catalysis. *ACS Catal.* **2018**, *8*, 4064–4081. [[CrossRef](#)]
35. Pizzutilo, E.; Kasian, O.; Choi, C.H.; Cherevko, S.; Hutchings, G.J.; Mayrhofer, K.J.J.; Freakley, S.J. Electrocatalytic Synthesis of Hydrogen Peroxide on Au-Pd Nanoparticles: From Fundamentals to Continuous Production. *Chem. Phys. Lett.* **2017**, *683*, 436–442. [[CrossRef](#)]
36. Huang, X.; Song, M.; Zhang, J.; Shen, T.; Luo, G.; Wang, D. Recent Advances of Electrocatalyst and Cell Design for Hydrogen Peroxide Production. *Nano-Micro Lett.* **2023**, *15*, 86. [[CrossRef](#)] [[PubMed](#)]
37. Chen, Z.; Wu, J.; Chen, Z.; Yang, H.; Zou, K.; Zhao, X.; Liang, R.; Dong, X.; Menezes, P.W.; Kang, Z. Entropy Enhanced Perovskite Oxide Ceramic for Efficient Electrochemical Reduction of Oxygen to Hydrogen Peroxide. *Angew. Chem.* **2022**, *134*, e202200086. [[CrossRef](#)]
38. Xia, Y.; Zhao, X.; Xia, C.; Wu, Z.-Y.; Zhu, P.; Kim, J.Y.; Bai, X.; Gao, G.; Hu, Y.; Zhong, J.; et al. Highly Active and Selective Oxygen Reduction to H₂O₂ on Boron-Doped Carbon for High Production Rates. *Nat. Commun.* **2021**, *12*, 4225. [[CrossRef](#)] [[PubMed](#)]
39. Xia, C.; Xia, Y.; Zhu, P.; Fan, L.; Wang, H. Direct Electrosynthesis of Pure Aqueous H₂O₂ Solutions up to 20% by Weight Using a Solid Electrolyte. *Science* **2019**, *366*, 226–231. [[CrossRef](#)]
40. Kim, H.W.; Ross, M.B.; Kornienko, N.; Zhang, L.; Guo, J.; Yang, P.; McCloskey, B.D. Efficient Hydrogen Peroxide Generation Using Reduced Graphene Oxide-Based Oxygen Reduction Electrocatalysts. *Nat. Catal.* **2018**, *1*, 282–290. [[CrossRef](#)]
41. An, J.; Feng, Y.; Zhao, Q.; Wang, X.; Liu, J.; Li, N. Electrosynthesis of H₂O₂ through a Two-Electron Oxygen Reduction Reaction by Carbon Based Catalysts: From Mechanism, Catalyst Design to Electrode Fabrication. *Environ. Sci. Ecotechnol.* **2022**, *11*, 100170. [[CrossRef](#)]
42. Jocić, A.; Breitenbach, S.; Bajuk-Bogdanović, D.; Pašti, I.A.; Unterweger, C.; Fürst, C.; Lazarević-Pašti, T. Viscose-Derived Activated Carbons Fibers as Highly Efficient Adsorbents for Dimethoate Removal from Water. *Molecules* **2022**, *27*, 1477. [[CrossRef](#)]
43. Bardestani, R.; Patience, G.S.; Kaliaguine, S. Experimental Methods in Chemical Engineering: Specific Surface Area and Pore Size Distribution Measurements—BET, BJH, and DFT. *Can. J. Chem. Eng.* **2019**, *97*, 2781–2791. [[CrossRef](#)]
44. Kupgan, G.; Liyana-Arachchi, T.P.; Colina, C.M. NLDFT Pore Size Distribution in Amorphous Microporous Materials. *Langmuir* **2017**, *33*, 11138–11145. [[CrossRef](#)] [[PubMed](#)]
45. Jocić, A.; Breitenbach, S.; Pašti, I.A.; Unterweger, C.; Fürst, C.; Lazarević-Pašti, T. Viscose-Derived Activated Carbons as Adsorbents for Malathion, Dimethoate, and Chlorpyrifos—Screening, Trends, and Analysis. *Environ. Sci. Pollut. Res.* **2022**, *29*, 35138–35149. [[CrossRef](#)]
46. Breitenbach, S.; Gavrilov, N.; Pašti, I.; Unterweger, C.; Duchoslav, J.; Stifter, D.; Hassel, A.W.; Fürst, C. Biomass-Derived Carbons as Versatile Materials for Energy-Related Applications: Capacitive Properties vs. Oxygen Reduction Reaction Catalysis. *C* **2021**, *7*, 55. [[CrossRef](#)]
47. Bard, A.J.; Faulkner, L.R. *Electrochemical Methods: Fundamentals and Applications*; Wiley: New York, NY, USA, 1980.
48. Milakin, K.A.; Gavrilov, N.; Pašti, I.A.; Morávková, Z.; Acharya, U.; Unterweger, C.; Breitenbach, S.; Zhigunov, A.; Bober, P. Polyaniline-Metal Organic Framework (Fe-BTC) Composite for Electrochemical Applications. *Polymer* **2020**, *208*, 122945. [[CrossRef](#)]
49. Vujković, M.; Gavrilov, N.; Pašti, I.; Krstić, J.; Travas-Sejdic, J.; Ćirić-Marjanović, G.; Mentus, S. Superior Capacitive and Electrocatalytic Properties of Carbonized Nanostructured Polyaniline upon a Low-Temperature Hydrothermal Treatment. *Carbon* **2013**, *64*, 472–486. [[CrossRef](#)]
50. Gavrilov, N.; Pašti, I.A.; Vujković, M.; Travas-Sejdic, J.; Ćirić-Marjanović, G.; Mentus, S.V. High-Performance Charge Storage by N-Containing Nanostructured Carbon Derived from Polyaniline. *Carbon* **2012**, *50*, 3915–3927. [[CrossRef](#)]
51. Gavrilov, N.; Vujković, M.; Pašti, I.A.; Ćirić-Marjanović, G.; Mentus, S.V. Enhancement of Electrocatalytic Properties of Carbonized Polyaniline Nanoparticles upon a Hydrothermal Treatment in Alkaline Medium. *Electrochim. Acta* **2011**, *56*, 9197–9202. [[CrossRef](#)]
52. Breitenbach, S.; Unterweger, C.; Lumetzberger, A.; Duchoslav, J.; Stifter, D.; Hassel, A.W.; Fürst, C. Viscose-based Porous Carbon Fibers: Improving Yield and Porosity through Optimization of the Carbonization Process by Design of Experiment. *J. Porous Mater.* **2021**, *28*, 727–739. [[CrossRef](#)]
53. Breitenbach, S.; Lumetzberger, A.; Hobisch, M.A.; Unterweger, C.; Spirk, S.; Stifter, D.; Fürst, C.; Hassel, A.W. Supercapacitor Electrodes from Viscose-Based Activated Carbon Fibers: Significant Yield and Performance Improvement Using Diammonium Hydrogen Phosphate as Impregnating Agent. *C* **2020**, *6*, 17. [[CrossRef](#)]

Disclaimer/Publisher's Note: The statements, opinions and data contained in all publications are solely those of the individual author(s) and contributor(s) and not of MDPI and/or the editor(s). MDPI and/or the editor(s) disclaim responsibility for any injury to people or property resulting from any ideas, methods, instructions or products referred to in the content.